The Egyptian Journal of Remote Sensing and Space Sciences 24 (2021) 353–360

HOSTED BY

Contents lists available at ScienceDirect

The Egyptian Journal of Remote Sensing and Space Sciences

journal homepage: www.sciencedirect.com

Identification of patterns associated with areas of epithermal alteration, through responses spectral using ASTER images

Jhonathan Aponte Saravia [a,b]

[a] Faculty of Natural Sciences and Engineering, Technological Units of Santander, Colombia
[b] Engineering and Services Los Andes SAS, Colombia

ARTICLE INFO

Article history:
Received 31 December 2019
Revised 10 June 2020
Accepted 15 June 2020
Available online 8 July 2020

Keywords:
Spectral indices
Mining exploration
Mineralization zones
Pattern identifications
Remote sensors

ABSTRACT

Knowing the potential of natural resources associated with mining activity is critical to decision-making especially at the exploration stage, this allows organizations to assess whether the area of interest is viable, to continue with post-exploration processes of mining deposits. So, it is important to get new exploration processes that cover very wide surfaces, be low-cost and reveal high reliability, one of these alternatives is the use of satellite imagery based on the principles of spectral responses. Therefore, The objective of the research was to search for a technique that considers the quantitative criteria to relate and identify the objects by using the spectral response values whose spectral response patterns are different, in an area whose cutting law for exploitation is feasible (zones of epithermal alteration), with the spectral response values of compounds associated with alteration zones of the United States Geological Survey (USGS), using two statistical criteria, correlation analysis and quadratic mean error, which have revealed good performance in identifying objects from the comparison of spectral responses.

1. Introduction

The inhabitants of the Andean region of Peru have been engaged in tasks related to goldsmithing since approximately 1700 years B. C. (Aldenderfer et al., 2008). This indicates that exploration and mining activities have developed since the Spanish invasion in the Inca Empire, increasing production significantly. Between 2006 and 2015, the production of this mineral has increased and now represents 5\% of world production and it is an important economic contribution for Peru (OSINERMING, 2017). In addition, the National Society of Mining, Petroleum and Energy (SNMPE) of Peru, reported a production of approximately 149.85 tons of gold in the year 2017. Moreover, mining is currently the economic sector that contributes most to Peru's gross domestic product.

On the other hand, the Peruvian Andes have scarce vegetation, which leaves the outcrops and the soil exposed. This allows the components of the soil surface to be assessed using indirect methods, the most applied method being the use of satellite images, specifically for mining exploration, agriculture applications and other purposes (Ninomiya, 2003; Sabbaghi & Moradzadeh, 2018). This method offers optimal results at this stage, since these data cover large areas and are available at low cost and others are free of charge. Furthermore, it is focused on the identification of areas with epithermal and hydrothermal alterations (Ninomiya, 2003; Sabbaghi & Moradzadeh, 2018; Sheikhrahimi et al., 2019).

In the last fifteen years, investigators have become interested in using satellite images for activities associated with mining exploration, as they have produced important results, especially hyperspectral and multispectral images such as the Advanced Spaceborne Thermal Emission and Reflection Radiometer (ASTER), launched in December 1999. This program captures surface data with fourteen bands in different spectral regions: three bands in the visible and near-infrared region, six in the mid-infrared region and five in the thermal region (Abrams et al., 2002). The bands in the mid-infrared and thermal regions have performed best in assessing geological resources, and in identifying areas with epithermal and hydrothermal alterations (Ninomiya, 2003; Pour & Hashim, 2012; Testa et al., 2018).

At the same time, some investigations have been focused on confirming and searching for new digital image processing techniques, using multispectral data to locate and explore hydrothermal and epithermal zones using various methods. In this sense, the Ratio Analysis, Mineralogical Indices, Band Combination, Principal Component Analysis (PCA), Minimum Noise Fraction, Pairwise Filter Processes, Spectral Profiling, have proven to be the most convenient methods (Gabr et al., 2010; Ji et al., 2011; Pour

Peer review under responsibility of National Authority for Remote Sensing and Space Sciences.
E-mail address: japonte@correo.uts.edu.co

https://doi.org/10.1016/j.ejrs.2020.06.005
1110-9823/

& Hashim, 2011). In addition, the ACP method, initially developed and applied for biophysical assessments, has also shown significant results in the mining exploration process (Loughlin, 1991; Zhang & Zhou, 2017).

On the other hand, the presence of clay minerals, associated with zones of hydrothermal and epithermal alteration, have shown certain features. For example, alunite [KAl3(SO4)2(OH)6] and jarosite [KFe33+(SO4)2(OH)6] are agglomerated within the group of sulphate minerals, where alunite formation occurs in volcanic environments as a result of intense leaching. It is also possible to find these compounds in the fumaroles and in areas of high sulfidation (Pirajno, 2009). The clay minerals associated with jarosite are usually formed due to the alteration of aluminum oxide (Al2O3) and silica (SiO2) compounds, which are found in felsic rocks —such as feldspars— after contact with acidic fluids (Dutrizac & Jambor, 2000).

The reflectance values for alunite and jarosite in the visible and near-infrared region are high, i.e. in bands 1, 2 and 3 of the ASTER image, and in bands 5 and 8 the reflectance values are low (Pour & Hashim, 2012; Modabberi et al., 2017; Rajendran & Nasir, 2017). Kaolinite has high values of reflectance in the near-infrared region, including the 1.4 um region, and reflectance is low in the mid-infrared region (Ninomiya, 2003; Modabberi et al., 2017; Masoumi et al., 2017). Also, compounds with predominant cations or positive ions (OH) or hydroxyl ion index (IHO) —mainly kaolinite, alunite and montmorillonite— show high absorption in band 6 of the ASTER image (Baldridge et al., 2009; Pour & Hashim, 2012). Furthermore, the reflectance of these clay minerals is high in band 4 and band 7 in the ASTER sensor images (Ninomiya, 2003; Baldridge et al., 2009; Pour & Hashim, 2012). In contrast, calcite in band 5 and band 8 of the ASTER image is highly absorbed (Ninomiya, 2003; Baldridge et al., 2009; Zhang & Zhou, 2017). Propylic-type mineralizations have high reflectance values in the 2.20 μm spectral region and high absorption in the 2.17 μm. This phenomenon occurs due to the high electron vibration in the minerals with predominance of (Fe-O-H), (Mg-O-H) and (CO3), making the absorption values also high in band 6 and band 8 of the ASTER image (Zhang & Zhou, 2017).

Some investigations have carried out interpretation based on the bands of the mid-infrared region, which has produced significant results (Ninomiya, 2003; Baldridge et al., 2009; Zhang & Zhou, 2017). However, few investigations have considered the participation of the mid-infrared and near-infrared bands, and these data also have a high potential to predict or identify objects from spectral responses. In this sense, the purpose of the research was to assess three comparison criteria. Quantitative data was used to identify the objects at the mining site, through spectral responses of different patterns captured by the ASTER image. Also, the spectral response of some components associated with epithermal and hydrothermal alteration zones from the United States Geological Survey (USGS) spectral library was used.

To reduce the levels of uncertainty in this process, a known area was chosen, where a mining company has been carrying out exploration and exploitation since 2008. This company has reported that the research area on average presents concentrations varying between 0.54 and 0.67 g of gold per ton (Seers et al., 2018). Therefore, this area is a strategic place to test algorithms and develop mining exploration methodologies using satellite images.

2. Materials and methods

2.1. Location

The area where the research was conducted is located in the Andean mountains. It shares borders with the states of Lima, Junín and Huancavelica, Peru, Fig. 1 sub-figure (a). Its geographical coordinates are 12°33′59,10″ S; 75° 34′13,87″ W and it is located at an average altitude of 4800 m above sea level (masl). The study zone is composed of Caudalosa (Nm-qua) geological formations, which are composed of interspersed andesitic flows, with andesitic breccias and tuffs; andesitic domes (N-dmand) formations originated by slow volcanic eruption processes; sacsaquero (P-s) formations, composed of gray porphyritic andesite, pinkish to brownish crystal tuffs and subordinate sandstones; glacier-type formations (Q-gl), composed of moraine deposits, angular blocks filled with clays, silts and sands; castrovirreyna formation (PN-cas), composed of andesites, agglomerates, tuffs and red sandstones. In the surrounding areas there are formations of this type: Goyllarisquizga group (Ki-g), Glacial deposit, fluvial (Q-glfl), Huayta volcanic center - andesite lava (N-huay-and); Huayta volcanic center - undifferentiated tuff (N-huay-tb) and others; image (b) of Fig. 1 (GEOCATMIN, 2019).

More detailed studies have found evidence of acidic volcanic rock formations, cylindrical volcanic breccias, pyroclasts and tuffs, typical zones of epithermal mineralization, composed by association of native silica sulphide minerals - porous alunite. In the higher parts there are silica outcrops (vuggy silica). There is a high probability of concentrations of alunite, jarosite, kaolinite, pyrophyllite and pyrite. These outcrops are aligned in a northwest-southwest direction. In addition, there is evidence of hydrothermal fluid systems, which are responsible for mineralization. They are located at the intersection of regional geological formations, specifically on fault lines running northwest to southwest and east to west (Seers et al., 2018).

2.2. Data

The data used in the investigation were satellite images from the ASTER sensor, which corresponds to the granule ASTB070608152833 captured on June 8, 2007. These data have 14 bands in different spectral regions, of which three bands in the infrared region and six bands in the near and mid-infrared region were used, even though mining activities had not yet started in the area of interest. These images were downloaded from the Japanese's Ministry of Economy, Trade and Industry (METI) satellite file system website, which is available at: https://gbank.gsj.jp/madas/map/index.html.

In addition, spectral response data was downloaded for some clay minerals highly associated with epithermal and hydrothermal alteration zones belonging to the sulphate group, such as kaolinite CM 511,846 (CAOL); alunite (ALU); muscovite GDS 107; (MUSCO); altered volcanic rock (AVR); alunite, kaolinite and muscovite (ACM) with proportions of 33% for each component; alunite (KNa) composed of potassium (K) and sodium (Na), with proportions of 35% and 65% respectively; alunite, muscovite and pyrollite (AMP) with proportions of 30%, 40% and 30% respectively; alunite and kaolinite (AC) with proportions of 50% for each component; ammonium and jarosite (AMJA) with proportions of 50% for each component; from the *United States Geological Survey* (USGS) spectral library, which is available at: https://pubs. usgs.gov/of/2003/ofr-03–395/datable.html as shown in image (c) of Fig. 2.

3. Method

3.0.1. Process from images

The satellite image data were initially in digital values, so it was necessary to convert them into reflectance values. The process consists of the transformation from digital level to radiance level, and

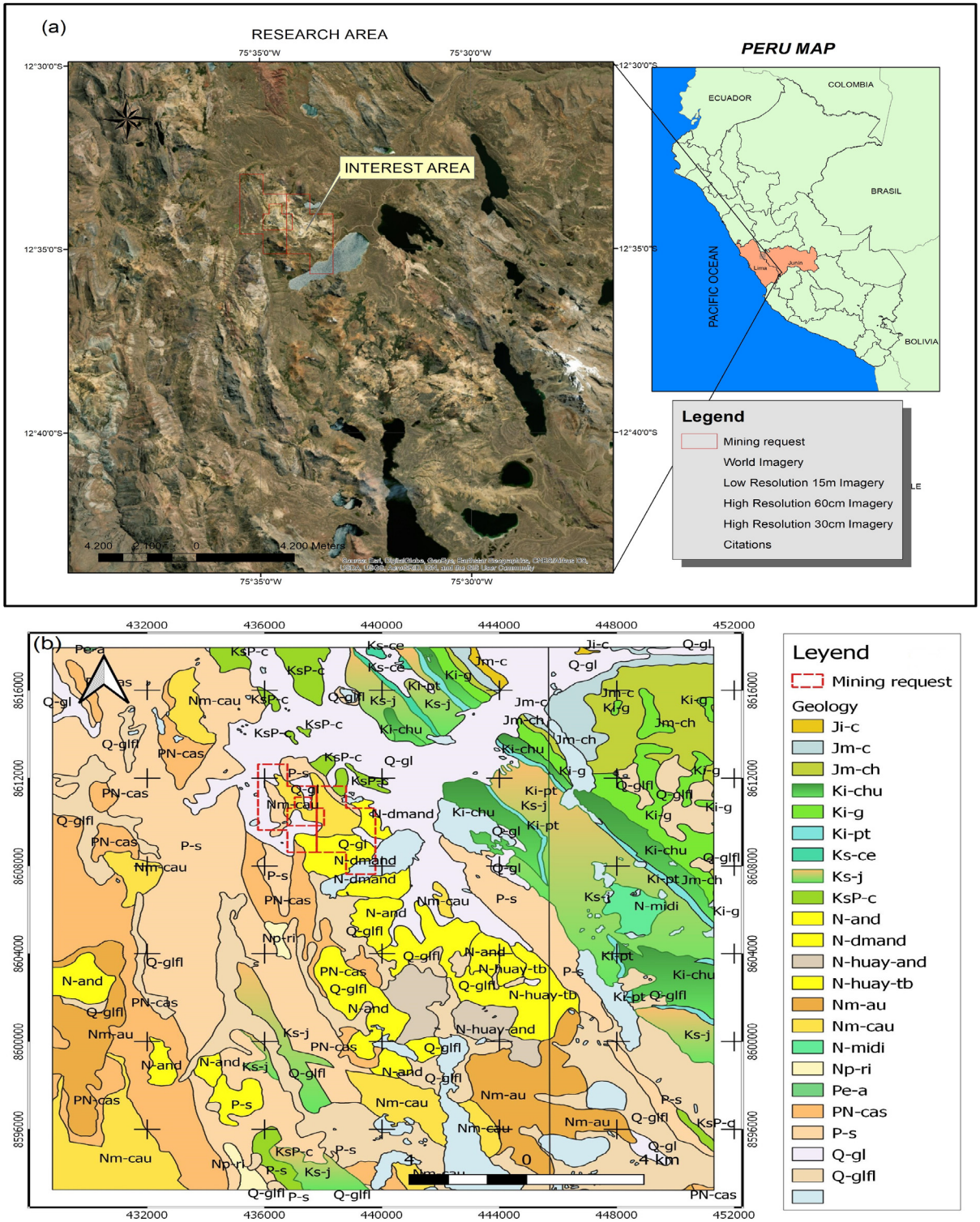

Fig. 1. (a) Indicates the location of the study area; (b) shows the map of geological units of the research area.

from radiance values to reflectance values (Abrams et al., 2002; Arai et al., 2010). This process was conducted using the program R Package, in order to obtain values of the pixels associated to the intrinsic property of the objects at surface level.

After confirming the correct conversion process of the reflectance values on the images, the RGB combination processes were performed using the bands (4, 3 and 2) respectively. This is due to the fact that this combination has made it possible to expose a greater number of tones to differentiate the objects, so that they can be differentiated visually more easily, as shown in image (a) in Fig. 2. Then, 50 pixels with similar spectral responses were selected. They were called patterns since they have similar spectral behaviors, image (a) of Fig. 2. Based on the data of each spectral region, the average value in each region of the spectrum was calculated, obtaining the average spectral response of each zone as shown in image (b) of Fig. 2.

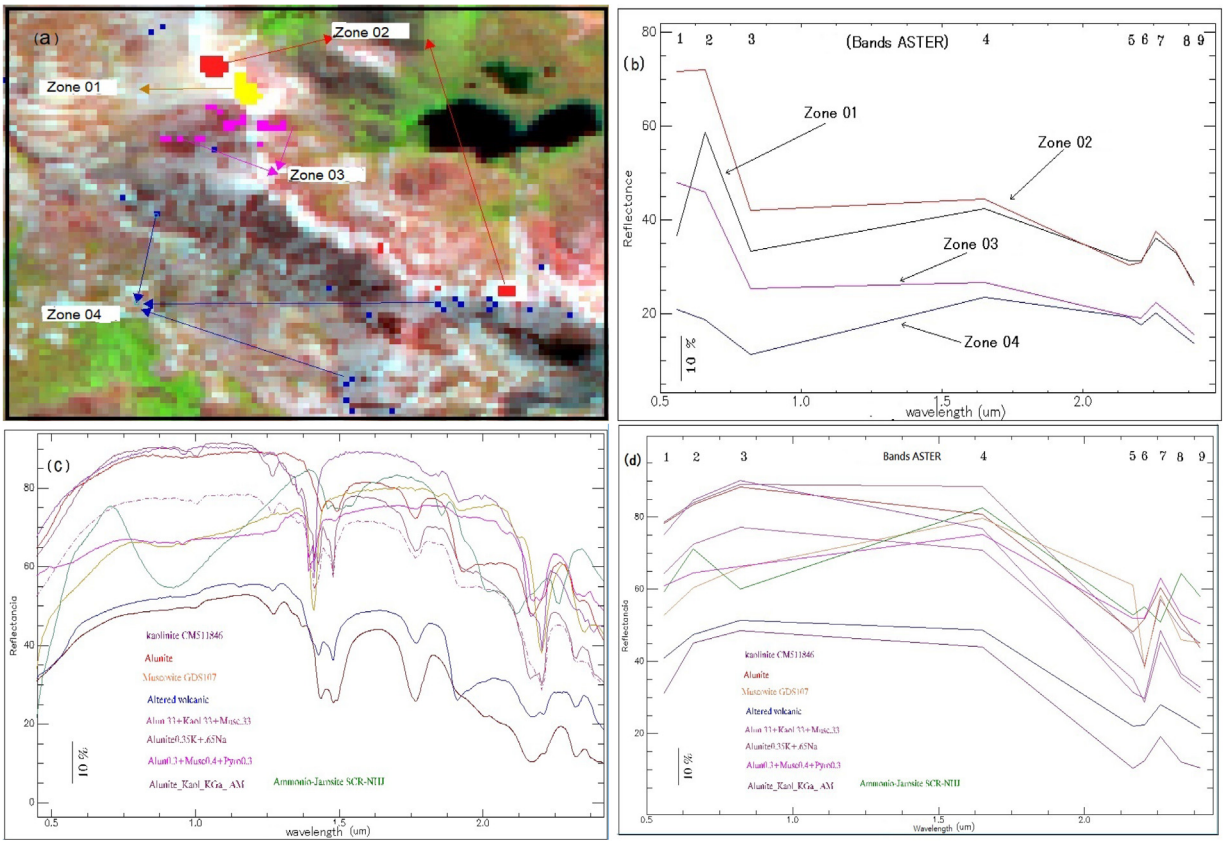

Fig. 2. Behavioral patterns of spectral responses of objects associated with epithermal and hydrothermal zones: a) indicates the location of the pixels selected for the evaluation of spec-tral responses; b) presents the patterns of spectral response behavior of the selected areas; c) the spectral response of some minerals of clay associated with epithermal and hydrothermal areas, source: USGS; d) present the pattern of simplified behavior of spectral responses de-rived from the USGS, of some clay minerals associated with epithermal and hydrothermal areas, which corresponds to the Average wavelength of the ASTER sensor bands.

3.0.2. Process from spectral signatures

The spectral response data from the USGS library were initially composed of very high spectral resolution values. Therefore, approximately 480 values of reflectance were generated between 0.205 μm and 2.976 μm, which allows the generation of a very detailed spectral response as shown in image (c) in Fig. 2. However, ASTER images between the mentioned region only show 9 values of reflectance. Thus, in order to compare these spectral responses, it was necessary to perform some previous operations.

First, the central value of the spectral region of each ASTER sensor band in the near and mid-infrared regions was calculated. After knowing the central values, those spectral regions were located in the spectral library of each selected compound to obtain the reflectance values of the compounds in nine spectral regions. In this way, simplified spectral responses derived from these compounds were obtained, from the spectral response of the USGS library as shown in image (d) of Fig. 2, with the purpose of comparing the reflectance values of the selected patterns in the ASTER image with the reflectance values of the USGS library, again showing this process in the ENVI academic version software.

3.0.3. Data comparison analysis

For the process of comparing reflectance values three comparison criteria were developed: first, the correlation analysis; second, the calculation of the mean squared error; and third, the equation of the *Spectral Angle Mapper* proposed by Kruse et al. (1993).

With this in mind, the processes for the calculation of the correlation analysis were carried out, applying equation (1). The mean spectral response values of the objects named (zones) were used with the spectral response values of the selected compounds from the USGS spectral library, see Fig. 2. This process was executed in the R Packages program. Prior to the above process, standardization tests were carried out, as the data analyzed did not have a normal distribution. Once the normalized data were obtained, the correlation analysis was performed by applying the following expression:

$$r = \frac{n\sum XiYi - \sum(Xi)\sum(Yi)}{\sqrt{n\sum X_i^2 - (\sum X_i^2)}\sqrt{n\sum Y_i^2 - (\sum Y_i^2)}} \quad (1)$$

where: r is the value of the correlation coefficient, X_i and Y_i are the values of the variables and n is the amount of data in the sample.

After having concluded the correlation analysis of the spectral response of the training zone against the spectral response of the compounds associated with epithermal and hydrothermal zones, the second statistical test, the *Root Mean Square Error* (RMSE), was carried out. This method has produced important results in the application of spatial data to assess the accuracy of proximity from one point to another (Perez et al., 1997; Michishita et al., 2012). The following expression was used:

$$D = \left\{ \left[\sum_i (Xi - X)\right]^2 + \left[\sum_i (Yi - Y)\right]^2 \right\}^{0.5} \quad (2)$$

where: D, is the average distance of the training data set from the test data set; X_i, Y_i are the mean values, X is the data set associated with wavelength values and Y is the data set associated with spectral response values.

To strengthen the interpretation of the results, the sum of the acute angles of the extremes, plus the sum of the lesser angles of the 360° turn of the vertices of the spectral responses of the pixels in the training area, was calculated and compared with the angles of the vertices of the spectral response of the objects associated with the test. This method has similar criteria to the algorithm developed by Kruse et al. (1993). This process was performed considering the criterion of Euclidean n-dimensional space (Marsden et al., 1991), which is expressed as follows:

$$\sum \theta = \sum ArCos \frac{v * \mu}{|v||\mu|} \quad (3)$$

where: θ, is the acute angle of the complement of the vertices that are located at the ends of the line of the spectral profile. In addition, θ is the lesser angle of the full 360-degree turn of the vertices that are located in the intervals of the spectral response; $v * \mu$ is the product of the vectors; and || v || y || μ ||, are the length of the vectors (Fig. 3).

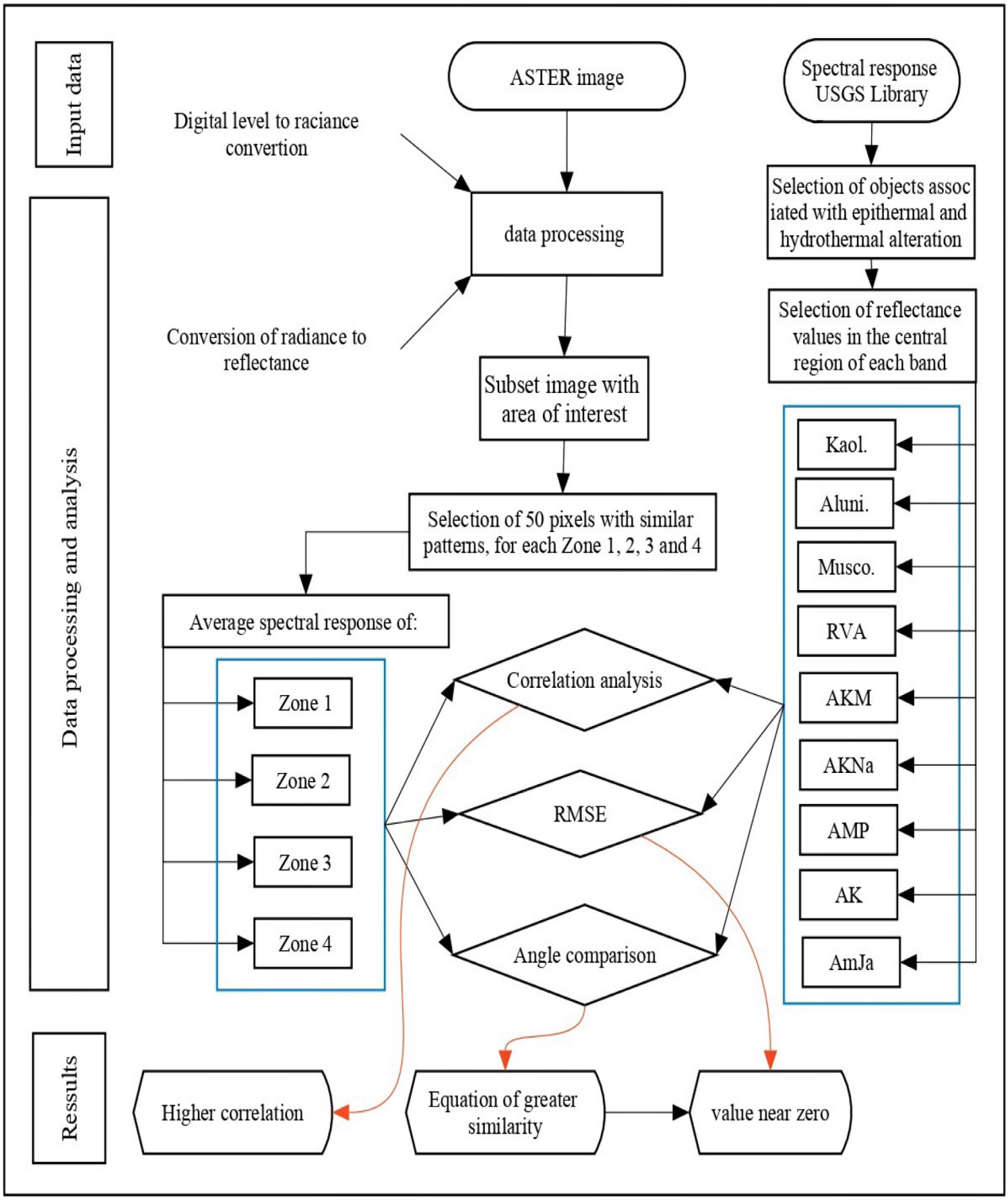

Fig. 3. Methodological scheme to identify patterns by spectral responses in epithermal and hydrothermal areas.

4. Results and discussions

The following are the most important results of the assessment for the identification of objects associated to epithermal alteration zones and their comparison with the spectral response of the training zones obtained from the ASTER image.

4.1. Spectral response analysis

The behavior of the spectral responses of the selected objects (zone 1, zone 2, zone 3 and zone 4) have different profile patterns, see image (b) in Fig. 2. In band 1 and band 2, the objects corresponding to zone 1 have a positive spectral slope; the objects in zone 2 have a slightly positive slope; and the reflectance values of zone 2 are high. This means that objects associated with the set of pixels have higher reflectivity (Rockwell, 2009). However, objects in zone 3 and zone 4 in the above-mentioned bands have negative spectral slopes.

From the visual analysis, the behavior of the spectral response of zone 1 shows some similarity with the spectral behavior of jarosite ammonium, where the slopes in band 1–2; band 2–3; band 3–4; band 4–5; band 7–8 and band 8–9 have values with the same sign, i.e. positive or negative slope. Also, zones 2 and 3 show similar slopes to the spectral response of ALU, AVR and AMP, between band 1–2, band 4–5, band 5–6, band 6–7, band 7–8 and band 8–9 respectively. This is also consistent with the spectral response reported by Rockwell (2009) in relation to clay minerals (alunite).

The absorption values of the training objects in the spectral region corresponding to band 3 (0.76–0.86) μm, were high with respect to band 1 (0.52–0.62) μm and band 2 (0.63–0.69) μm. This differs from the spectral behavior of the test objects. However, the spectral response patterns in the mid-infrared region of the objects associated with training zones, with the test objects, had more similarity considering the visual analysis criterion. That is, the absorption values in band 4 (1.60–1.70) μm were low for all training zones, evidencing less absorption in zone 2.

In band 5 (2,145–2,185) μm and band 6 (2185–2225) μm the absorption values were higher. This is consistent with the findings of (Modabberi et al., 2017), who associate them to alunite and kaolinite and montmorillonite. On the other hand, absorption values in band 7 (2235–2285) μm for all samples were high, evidencing less absorption in zone 2. In band 8 and band 9 the absorption values were also high, confirming the findings of (Modabberi et al., 2017; Masoumi et al., 2017), who associate them with muscovite, kaolinite, montmorillonite and alunite.

4.2. Correlation analysis

From the correlation analysis of the spectral responses of the objects associated to zones 1, 2, 3 and 4, against the spectral response of the objects associated to clay minerals —which have a high probability of being located in epithermal and hydrothermal zones— it was found that zone 2 has high correlation with the clay minerals of AC, ALU and ACM, whose values are: 0.76 , 0.75 , 0.73 respectively. Likewise, zone 3 also shows a close relationship with AC and ALU, this value being 0.72 for each compound, see Table 1.

Also, some training zones —such as zone 1, zone 2 and zone 3— show relatively high or moderate correlation (Martínez Ortega et al., 2009) with CAOL, AVR, and ACM clay minerals, as shown in Table 1. Thus, it allows to confirm what was found (existence of alunite and quartzite and high-sulphidation oxides on the surface of the study area) in the technical report submitted by the organization currently engaged in the mining process (Seers et al., 2018).

4.3. Root mean square error (RMSE) analysis

Based on the RMSE assessment of the spectral response of the objects associated with the training zones (zone 1, zone 2, zone 3 and zone 4), compared to the spectral response of the objects associated with a high probability of clay minerals in epithermal and hydrothermal alteration zones, the one with the least bias in zone 1 corresponds to the minerals associated with jarosite ammonium (sulphate group), and is probably related to a high polymetallic mineralization (Gonzales, 2015). The same is true for AMP compounds, which correspond to areas of advanced argillic alteration, see Table 2. Similarly, characterization studies have revealed the existence of gold and silver in the research area (Seers et al., 2018).

Zone 2 and Zone 3 have less bias with the clay minerals associated with AC and ALU, whose values are 0.073 and 0.077 for Zone 2 and 0.085 and 0.090 for Zone 3, respectively. Similarly, there is less deviation with compounds associated with ACM and RVA. This again confirms the results of this statistical method, with results that have been revealed in the detailed characterization studies conducted by the organization currently performing the mining processes (Seers et al., 2018).

4.4. Analysis of angle calculation through vectors

Based on the analysis of Table 3, the sum of the lesser angles of the vertices, both of the complement and the conjugate, show

Table 1
Correlation of spectral response values of some components that correspond to areas of epithermal alteration, with values of spectral responses of areas of training.

	CAOL.	ALU.	MUSCO RVA		ACM	AKNa	AMP	AC	AMJA
Zona1	0.63	0.65	0.44	0.64	0.65	0.67	0.59	0.65	0.60
Zona2	0.71	0.75	0.28	0.69	0.73	0.67	0.50	0.76	0.38
Zona3	0.68	0.72	0.24	0.65	0.69	0.63	0.45	0.72	0.33
Zona4	0.16	0.12	0.37	0.10	0.12	0.07	0.39	0.06	0.36

Table 2
Presents the mean square error (RSME) values, calculated between the values of spectral response derived from the spectral library, with respect to the response values spec-tral of the selected areas.

Zonas	CAOL.	ALU	MUSCO RVA		ACM	AKNa	AMP	AC	AMJA
Zona 1	404.18	332.14	455.42	277.96	378.14	244.10	331.72	307.82	285.22
Zona 2	296.90	249.08	378.88	180.46	280.12	225.52	243.24	246.42	279.24
Zona 3	316.60	221.77	354.67	135.81	272.52	199.45	226.53	210.33	337.49
Zona 4	263.12	183.89	338.28	94.40	266.78	234.40	176.82	239.36	355.78

Table 3
Presents the values of the difference of the sum of the angles of the vertices of objects associated with test areas with training objects.

Zonas	CAOL.	ALU	MUSCO RVA		ACM	AKNa	AMP	AC	AMJA
Zona 1	404.18	332.14	455.42	277.96	378.14	244.10	331.72	307.82	285.22
Zona 2	296.90	249.08	378.88	180.46	280.12	225.52	243.24	246.42	279.24
Zona 3	316.60	221.77	354.67	135.81	272.52	199.45	226.53	210.33	337.49
Zona 4	263.12	183.89	338.28	94.40	266.78	234.40	176.82	239.36	355.78

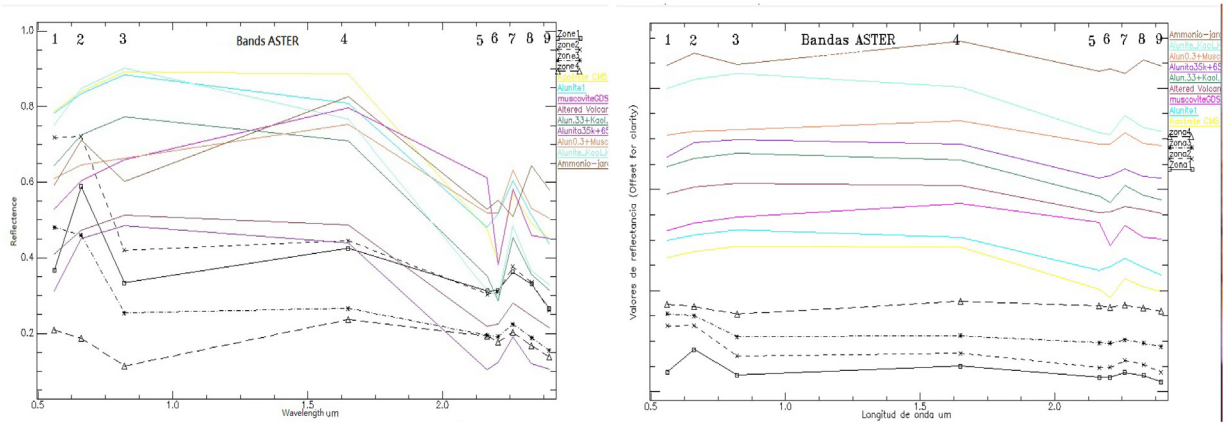

Fig. 4. shows the spectral responses of the training objects called as (zones) and the spec-tral responses of objects called as evidence.

greater similarity between zone 4, zone 3, zone 2 and RVA. Also, there is a certain level of similarity between zone 4 and AMP, zone 3 and AKNa. The most biased are the spectral response angles of zone 1 with muscovite and kaolinite, zone 3 with MUSCO and with AMJA, and zone 4 with AMJA. However, there is no similarity between the angles and the objects within the research area (alunite) (Seers et al., 2018).

The inconsistency of the angles between the test objects and the training objects is probably due to the definition of the inflection point in a very sharp region of the spectrum (spectral region defined as the inflection point, spectral response associated with the central value of the wavelength of each ASTER sensor band). This is because the spectral response of the objects captured by the ASTER sensor, called training zones, are average values captured in relatively large regions (the width of the sections of the spectral regions is greater than 40 nm). In contrast, the spectral response of the test objects have values in very short sections of the spectral regions, approximately every two nanometers (Figs. 3 and 4).

5. Conclusions

Statistical tests of Pearson's correlation analysis and root mean square analysis showed similar results, suggesting a high probability of compounds associated with ALU, AC of proportions of 50% for each component, in zone 2 and zone 3, respectively. This is consistent with the information described in the studies conducted by the organization that currently carries out the mining processes.

Angle comparison analysis in band 1 and band 9 and conjugate angles in the regions of the bands located in the intermediate did not produce significant results in the identification of objects through comparison. On the contrary, it creates a greater uncertainty regarding the comparison of spectral responses.

This technique has produced important results in the process of identifying epithermal and hydrothermal alteration zones. In this sense, it is convenient to carry out the validation in other areas, where the features of the object being studied are similar to the evaluated area.

The data captured by the ASTER sensor comprise an important source for mining exploration studies, since they allow efficient identification of areas with high potential for epithermal and hydrothermal alteration. Likewise, they allow the recognition of large areas, making the exploration processes associated with mining and geological management more efficient and cost-effective from a technical approach.

Declaration of Competing Interest

The authors declare that they have no known competing financial interests or personal relationships that could have appeared to influence the work reported in this paper.

References

Abrams, M., Hook, S., & Ramachandran, B. (2002). Aster user hand book. Pasadena, CA: Jet Propulsion Laboratory, 1–135. Retrieved from http://landcover.org/library/pdf/asteruserguidev2:pdf.

Aldenderfer, M., Craig, N.M., Speakman, R.J., Popelka-Filcoff, R., 2008. Four-thousand year-old gold artifacts from the lake titicaca basin, southern peru. Proc. Natl. Acad. Sci. 105 (13), 5002–5005. https://doi.org/10.1073/pnas.0710937105.

Arai, K., Thome, K., Iwasaki, A., Biggar, S., 2010. Aster vnir and swir radiometric calibration and atmospheric correction. Springer, New York, NY 83 (116). https://doi.org/10.1007/978-1-4419-6749-75.

Baldridge, A.M., Hook, S., Grove, C., Rivera, G., 2009. The aster spectral library version 2.0. Remote Sens. Environ. 113 (4), 711–715. https://doi.org/10.1016/j.rse.2008.11.007.

Dutrizac, J.E., Jambor, J.L., 2000. 01). Jarosites and their application in hydrometallurgy. Rev. Mineral. Geochem. 40 (1), 405–452. https://doi.org/10.2138/rmg.2000.40.8.

Gabr, S., Ghulam, A., Kusky, T., 2010. Detecting areas of high-potential gold mineralization using aster data. Ore Geol. Rev. 38 (1), 59–69. https://doi.org/10.1016/j.oregeorev.2010.05.007.

GEOCATMIN. (2019). Sistema de información geológico y catastral minero. Instituto Geológico, Minero y Metalúrgico, –. Retrieved from https://geocatmin.ingemmet.gob.pe/geocatmin/.

Gonzales, C. V. (2015). Caracterización espectral de tipos de alunita y silice en depósitos epitermales de alta sulfuración utilizando imágenes aster. Anais XVII Simpósio Brasileiro de Sensoriamento Remoto-SBSR, 547.

Ji, L., Zhang, L., Wylie, B.K., Rover, J., 2011. On the terminology of the spectral vegeta tion index (nirswir)/(nir+swir). Int. J. Remote Sens. 32 (21), 6901–6909. https://doi.org/10.1080/01431161.2010.510811.

Kruse, F. A., Lefkoff, A., Boardman, J., Heidebrecht, K., Shapiro, A., Barloon, P., & Goetz, A. (1993). The spectral image processing system (sips)-interactive

visualization and analysis of imaging spectrometer data. In Aip conference proceedings (Vol. 283, pp. 192–201).
Loughlin, W. (1991). Principal component analysis for alteration mapping. Photogrammetric Engineering and Remote Sensing, 57(9), 1163–1169. Retrieved from https://www.asprs.org/wp-content/uploads/pers/1991journal/sep/1991_sep_1163-1169.pdf.
Marsden, J. E., Tromba, A. J., & Mateos, M. L. (1991). Cálculo vectorial (Vol. 69). Addison- Wesley Iberoamericana.
Martínez Ortega, R.M., Tuya Pendás, L.C., Martínez Ortega, M., Pérez Abreu, A., Cánovas, A.M., 2009. El coeficiente de correlación de los rangos de spearman caracterización. Revista Habanera de Ciencias Médicas 8 (2).
Masoumi, F., Eslamkish, T., Honarmand, M., Abkar, A.A., 2017. Utilization of aster data and spectral analysis to discriminate hydrothermally altered areas over rabor, south of kerman, iran. J. Indian Soc. Remote Sens. 45 (6), 1039–1055.
Michishita, R., Gong, P., Xu, B., 2012. Spectral mixture analysis for bi-sensor wetland mapping using landsat tm and terra modis data. Int. J. Remote Sens. 33 (11), 3373–3401. https://doi.org/10.1080/01431161.2011.611185.
Modabberi, S., Ahmadi, A., Tangestani, M.H., 2017. Sub-pixel mapping of alunite and jarosite using aster data; a case study fromnorth of semnan, north central iran. Ore Geol. Rev. 80, 429–436. https://doi.org/10.1016/j.oregeorev.2016.07.014.
Ninomiya, Y., 2003. A stabilized vegetation index and several mineralogic indices defined for aster vnir and swir data. IEEE 3, 1552–1554. https://doi.org/10.1109/IGARSS.2003.1294172.
OSINERMING. (2017). La industria de la minería en el perú. 1(1), 1–166. Retrieved from https://www.osinergmin.gob.pe/seccion/centro_documental/mineria/Documentos/Publicaciones/Osinergmin-Industria-Mineria-Peru-20anios.pdf.
Perez, R., Seals, R., Zelenka, A., 1997. Comparing satellite remote sensing and ground network measurements for the production of site/time specific irradiance data. Sol. Energy 60 (2), 89–96. https://doi.org/10.1016/S0038-092X(96)00162-4.
Pirajno, F. (2009). Hydrothermal processes and wall rock alteration. In Hydrothermal processes and mineral systems (pp. 73–164). doi: 10.1007/978-1-4020-8613-72.
Pour, A.B., Hashim, M., 2011. Spectral transformation of aster data and the discrimination of hydrothermal alteration minerals in a semi-arid region, se iran. International Journal of the Physical Sciences 6 (8), 2037–2059.
Pour, A.B., Hashim, M., 2012. The application of aster remote sensing data to porphyry copper and epithermal gold deposits. Ore Geol. Rev. 44, 1–9. https://doi.org/10.1016/j.oregeorev.2011.09.009.
Rajendran, S., Nasir, S., 2017. Characterization of aster spectral bands for mapping of alteration zones of volcanogenic massive sulphide deposits. Ore Geol. Rev. 88, 317–335. https://doi.org/10.1016/j.oregeorev.2017.04.016.
Rockwell, B. W. (2009). Comparison of aster-and aviris-derived mineraland vegetation maps of the white horse replacement alunite deposit and surrounding area, marysvale volcanic field, utah (Tech. Rep.). US Geological Survey. doi: 10.3133/sir20095117.
Sabbaghi, H., Moradzadeh, A., 2018. Aster spectral analysis for host rock associated with porphyry copper-molybdenum mineralization. J. Geol. Soc. India 91, 627–638. https://doi.org/10.1007/s12594-018-0914-x.
Seers, D., Fowler, A., Espinoza, R., & Jouhston, A. (2018). Updated ni 43-101 technical reportminera irl limited corihuarmimine. Minera IRL Limited, 2(1), 1-181. Retrieved from https://www.minera-irl.com/files/2019-pdf/NI_43-101_TECHNICAL_REPORT.pdf.
Sheikhrahimi, A., Pour, A. B., Pradhan, B., & Zoheir, B. (2019). Mapping hydrothermal alteration zones and lineaments associated with orogenic gold mineralization using aster data: A case study from the sanandaj-sirjan zone, iran. Adv. Space Res., 63(10), 425 3315–3332. doi: 10.1016/j.asr.2019.01.035.
Testa, F. J., Villanueva, C., Cooke, D. R., & Zhang, L. (2018). Lithological and hydrothermal alteration mapping of epithermal, porphyry and tourmaline breccia districts in the argentine andes using aster imagery. Remote Sensing, 10 (203), 627–638. doi: 429 10.3390/rs10020203.
Zhang, N., Zhou, K., 2017. Identification of hydrothermal alteration zones of the baogutu porphyry copper deposits in northwest china using aster data. J. Appl. Remote Sens. 11, (1). https://doi.org/10.1117/1.JRS.11.015016 015016.